

A nonvolatile magnon field effect transistor at room temperature

Received: 3 December 2023

Accepted: 14 October 2024

Published online: 29 October 2024

 Check for updates

Jun Cheng ^{1,6}, Rui Yu^{1,2,6}, Liang Sun ^{1,6}, Kang He¹, Tongzhou Ji¹, Man Yang ¹, Zeyuan Zhang¹, Xueli Hu¹, Heng Niu ¹, Xi Yang¹, Peng Chen¹, Gong Chen ¹, Jiang Xiao ³, Fengzhen Huang ¹, Xiaomei Lu ¹, Hongling Cai ¹, Huaiyang Yuan ⁴ , Bingfeng Miao ¹  & Haifeng Ding ^{1,5} 


Information industry is one of the major drivers of the world economy. Its rapid growth, however, leads to severe heat problem which strongly hinders further development. This calls for a non-charge-based technology. Magnon, capable of transmitting spin information without electron movement, holds tremendous potential in post-Moore era. Given the cornerstone role of the field effect transistor in modern electronics, creating its magnonic equivalent is highly desired but remains a challenge. Here, we demonstrate a nonvolatile three-terminal lateral magnon field effect transistor operating at room temperature. The device consists of a ferrimagnetic insulator ($\text{Y}_3\text{Fe}_5\text{O}_{12}$) deposited on a ferroelectric material [$\text{Pb}(\text{Mg}_{1/3}\text{Nb}_{2/3})_{0.7}\text{Ti}_{0.3}\text{O}_3$ or $\text{Pb}(\text{Zr}_{0.52}\text{Ti}_{0.48})\text{O}_3$], with three Pt stripes patterned on $\text{Y}_3\text{Fe}_5\text{O}_{12}$ as the injector, gate, and detector, respectively. The magnon transport in $\text{Y}_3\text{Fe}_5\text{O}_{12}$ can be regulated by the gate voltage pulses in a nonvolatile manner with a high on/off ratio. Our findings provide a solid foundation for designing energy-efficient magnon-based devices.

Since the 1960s, the density of transistors in integrated circuits has followed Moore's law, doubling approximately every two years. However, with the increasing density and speed of the devices, the density of the power consumption also increases, resulting in a growing serious heat problem. This obstacle strongly limits the further development of integrated circuits¹. In order to overcome this problem, it becomes imperative to explore alternative possibilities instead of solely relying on the charge property of the electrons. Magnon, a collective excitation of magnetic moments, can carry spin information without electron movement, i.e., in the absence of the Joule heating^{2–10}. Besides, magnon can also enable the switching of magnetization¹¹. These remarkable features make magnon one of the most promising information carriers in post-Moore era^{2,9,12–19}. Given the prominent role of the field effect transistor (FET) in modern electronics, it is highly

desirable to create its corresponding magnonic version. However, unlike the charge currents in semiconductors which can be readily regulated with an electric field, finding an equivalent method for controlling magnon current is very challenging due to the weak coupling between the electric field and magnetic moment because of their different symmetry requirements²⁰. Though there are several theoretical and experimental investigations on the electric field induced frequency shift of the spin waves^{21,22}, the control of the magnon flow with an electric field has yet to be reported.

In the hot pursuit of manipulation of magnon transport, different versions of magnon transistors have been demonstrated^{23–33}. These devices either transmit magnon current vertically or rely on gating with the electric current or magnetic field^{31–33}. The magnonic circuits, however, require the magnon transistor to be in lateral structure and

¹National Laboratory of Solid State Microstructures and Department of Physics, Nanjing University, and Collaborative Innovation Center of Advanced Microstructures, Nanjing 210093, PR China. ²Shanghai Advanced Research Institute, Chinese Academy of Sciences, Shanghai 201204, PR China. ³Department of Physics, Fudan University, Shanghai 200433, PR China. ⁴Institute for Advanced Study in Physics, Zhejiang University, 310027 Hangzhou, PR China. ⁵Shishan Laboratory, Suzhou Campus of Nanjing University, Suzhou 215000, PR China. ⁶These authors contributed equally: Jun Cheng, Rui Yu, Liang Sun.

 e-mail: hyyuan@zju.edu.cn; bfmiao@nju.edu.cn; hfding@nju.edu.cn

have three terminals for device cascading, ideally having high energy efficiency such as being controlled by electric field and nonvolatile. Despite successfully controlling magnon current through the magnon-magnon scattering²³ and switching the magnetization beneath the detector³⁰, developing a three-terminal electric field controlled lateral magnon FET still remains a grand challenge.

Here, we report a unique design and the experimental demonstration of a nonvolatile three-terminal lateral magnon FET. By applying electric field pulses at the gate, a strong modulation of the thermally excited magnon current laterally propagating from the source to the detector is achieved at room temperature. A high on/off ratio up to ~400% is observed. Importantly, our device operates in a nonvolatile manner at room temperature and with the electric field gating. This notable progress demonstrates the capabilities of the three-terminal magnon FET, enabling the development of innovative and energy-efficient solutions. Our results not only open doors to electric field controlled, low-power-consumption magnon-based conventional logic computing, but also reveal potential applications in neuromorphic computing.

Results

The operational principle

Figure 1 presents a brief sketch of our design of the magnon FET. The device consists of three parallel heavy metal (HM) nano-strips on top of a ferromagnetic or ferrimagnetic insulator (FI) film deposited on a ferroelectric (FE) material. The nano-strips serve as the magnon source (S), gate (G), and detector (D), respectively. When a charge current passes through the S-stripe, magnons are excited by the spin current via the spin Hall effect (SHE) in HM and the thermal activation. The imbalanced distribution of the magnon results in a lateral magnon current propagating from the S-stripe toward the D-stripe. When voltage pulses with sufficient intensities are applied, the electric polarization of the ferroelectric domain beneath the G-stripe can be modulated. The coupling between the FI film and the FE layer subsequently has a substantial impact on the propagation of the magnon current from the S- to D-stripe, resulting in a “high” or “low” non-local voltage V_{nl} across the D-stripe, which can be detected via the inverse spin Hall effect (ISHE) in HM.

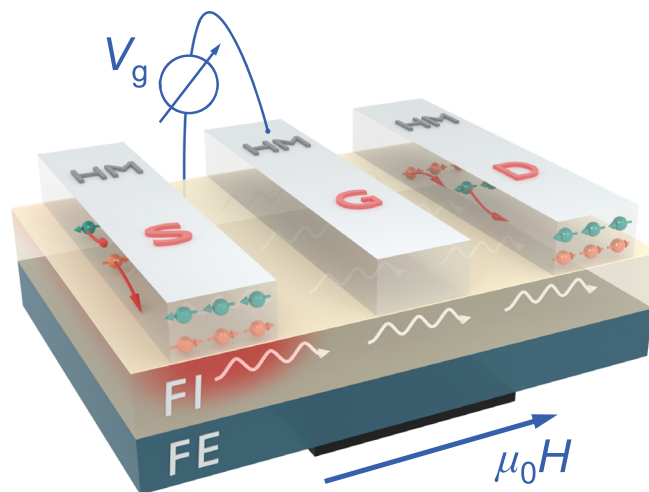


Fig. 1 | Sketch of a three-terminal magnon field effect transistor (Magnon FET). Three heavy-metallic (HM) stripes are placed onto a ferromagnetic or ferrimagnetic insulator (FI) /ferroelectric (FE) bilayer. The left stripe acts as the magnon source (S), while the transmission of magnons to the detector (D) stripe placed on the right side can be modulated by the voltage pulses V_g applied at the gate (G) stripe, which is located in the middle. Meanwhile, spin accumulation is generated at the HM/FI

interface of the injector stripe via the spin Hall effect or thermal excitation, and the spin accumulation is converted into a charge current at the detector stripe through the inverse spin Hall effect. Additionally, a bottom electrode is positioned beneath the FE layer and is aligned with the G-stripe. The magnetic field $\mu_0 H$ is applied in the film plane. In our experiments, the materials of HM, FI, and FE are selected as Pt, $Y_3Fe_5O_{12}$, and $Pb(Mg_{1/3}Nb_{2/3})_{0.7}Ti_{0.3}O_3$ or $Pb(Zr_{0.52}Ti_{0.48})O_3$, respectively.

Non-local measurements of the lateral magnon transport

We first established a non-local measurement for the magnon transport. Figure 2a shows a scanning electron microscopy (SEM) image of a typical device, which consists of only the S- and D-strips. The center-to-center distance between the two stripes is d , and the in-plane external magnetic field is applied with an angle α with respect to the perpendicular direction of the stripe, as marked in the inset. We applied a low-frequency ($f = 15.7$ Hz) AC current with an amplitude of $I_\omega = 0.71$ mA in the S-stripe and measured the first ($V_{nl}^{1\omega}$) and second ($V_{nl}^{2\omega}$) harmonic non-local voltages at the D-stripe as a function of α with a lock-in amplifier. Figure 2b, c presents the angular dependence of $V_{nl}^{1\omega}$ and $V_{nl}^{2\omega}$ for $d = 2$ μ m, respectively. Together with the I_ω -dependent studies (Supplementary Note 3), the corresponding fittings show that these non-local voltages can be well described by $V_{nl}^{1\omega} \propto I_\omega \cos^2 \alpha$ and $V_{nl}^{2\omega} \propto I_\omega^2 \cos \alpha$, respectively. These results are consistent with previous findings^{3,31}, and show that $V_{nl}^{1\omega}$ originates from the electronically injected magnon current via the SHE and $V_{nl}^{2\omega}$ is due to the magnon current thermally excited via the spin Seebeck effect (SSE). We note our obtained phase difference between 1ω - and 2ω -curves is the same as ref. 3 but has a shift of π with ref. 31, which may be due to the opposite definition of the injected current direction.

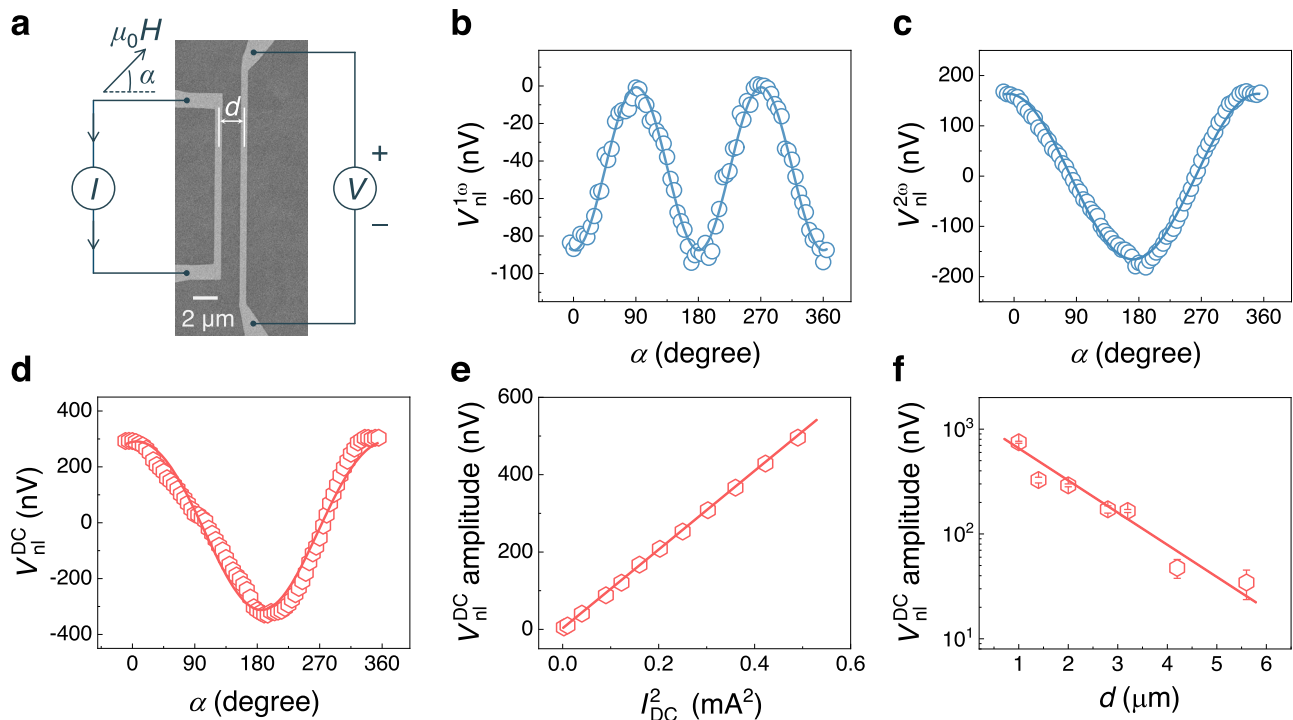


Fig. 2 | Non-local measurements of the lateral magnon transport. **a** Scanning electron microscope image of a typical device for non-local detection of the magnon transport with a two-terminal configuration. The left Pt-stripe serves as the magnon source, while the right one is the detector. The center-to-center distance between the two stripes is d . α denotes the angle between the direction of the applied magnetic field $\mu_0 H$ and the direction perpendicular to the stripes. **b**, **c** Angular dependence of the simultaneously measured first- and second-harmonic non-local voltage signals, respectively. The lines are the fittings with the

$\cos^2 \alpha$ and $\cos \alpha$ functions, respectively. **d** Angular dependence of the DC non-local voltage signal. The line is the fitting obtained with the sum of both $\cos \alpha$ and $\cos^2 \alpha$ functions. The best fitting yields their relative ratio in amplitude to be $\sim 13:1$. **e** Dependence of the DC non-local voltage amplitude with the square of DC current. The line is a linear fitting. **f** DC non-local voltage amplitude (in the logarithmic scale) as a function of d . Error bars are obtained from repeated measurements for each d . The line is a linear fitting. In **b**–**f**, the symbols are the experimental data.

To circumvent the obstacle induced by capacitive and inductive couplings and explicitly demonstrate the electric field gating effect on the magnon transport, we also performed the non-local measurements with the DC injected current I_{DC} . In principle, the detected non-local voltage V_{nl}^{DC} (measured with a voltmeter) corresponds to the combined effect induced by both the electrically and thermally generated magnons. Due to the different time scales between the electron and thermal relaxation, the contribution from the thermally generated magnons is expected to increase with decreasing frequency^{38,39}. Indeed, the obtained V_{nl}^{DC} is dominated by the angular dependence of $\cos \alpha$ for the DC measurements ($f \cong 0$ Hz) (Fig. 2d). This is further supported by the power-dependent measurement (Fig. 2e), which shows that V_{nl}^{DC} amplitude is proportional to the square of the applied DC current, I_{DC}^2 . We also fabricate a series of devices with different distance d between the S- and D-strips as marked in Fig. 2a. The measured V_{nl}^{DC} amplitude shows an exponential decay with d (Fig. 2f). The extracted magnon diffusion length $\lambda = 1.42 \pm 0.20 \mu\text{m}$ is slightly shorter than that obtained in the epitaxial YIG films^{3,40}, as expected for the sputtered polycrystalline films.

Demonstration of the magnon FET

To study the electric field controlled magnon transport in the YIG channel, we prepared the samples with all the S-, G-, and D-strips. Figure 3a shows an SEM image of a typical device. A voltage pulse V_g is applied at the G-stripe, and the modulation of the magnon propagation is measured via the voltage change at the D-stripe. Before the electric field dependent measurements, several cycles of sweeping V_g between -200 V and $+200$ V were performed to reduce the memory effect. We first measured the non-local voltage V_{nl}^{DC} as a function of the in-plane magnetic field $\mu_0 H$ ($\alpha = 0$) under different applied voltage

pulses (Fig. 3b, c). We note that all curves were obtained after the electric field had been removed, namely in a nonvolatile manner. When $V_g = +200$ V, V_{nl}^{DC} exhibits a hysteresis loop with an amplitude (defined as half the difference between V_{nl}^{DC} obtained under positive and negative saturation magnetic field) of ~ 130 nV. This behavior is consistent with the thermally generated magnon current, as the electrically generated magnon current exhibits a $\cos^2 \alpha$ -angle-dependence and remains unaffected by changing the magnetic field direction. We find that the magnetic-field-dependent V_{nl}^{DC} exhibits an enhancement near the coercivity ($H_C \sim 2.4$ mT). A similar phenomenon was observed previously, though its origin was not mentioned⁴¹. We proposed a possible explanation for this phenomenon (see Supplementary Note 4). When V_g decreases from $+200$ V to -10 V, the amplitude of V_{nl}^{DC} remains almost unchanged. In contrast, with further decreasing V_g the amplitude of V_{nl}^{DC} first decreases gradually and goes more sharply near $V_g = -100$ V, and eventually becomes negligibly small when V_g is below -110 V. In this process, we also observed a change in the shape of the hysteresis loop, indicating a change in magnetic anisotropy. Increasing V_g from -200 V back to $+200$ V gives the reverse behavior. The amplitude of V_{nl}^{DC} does not change significantly when V_g is increased to $+10$ V, and a sharp increase occurs around $V_g = +150$ V. The curve almost recovers the initial state when V_g returns to $+200$ V. We also calculated the charge loop (blue curve in Fig. 3b) with the V_g -dependent leakage current⁴² and found that they exhibited close similarity, indicating a strong correlation between the observed magnon current modulation and the change of the electric polarization of the FE layer.

Figure 3b summarizes the electric control of the amplitude of the non-local voltage V_{nl}^{DC} in the magnon FET. The V_{nl}^{DC} amplitude shows an almost square-shaped electric hysteresis loop, with a larger (smaller)

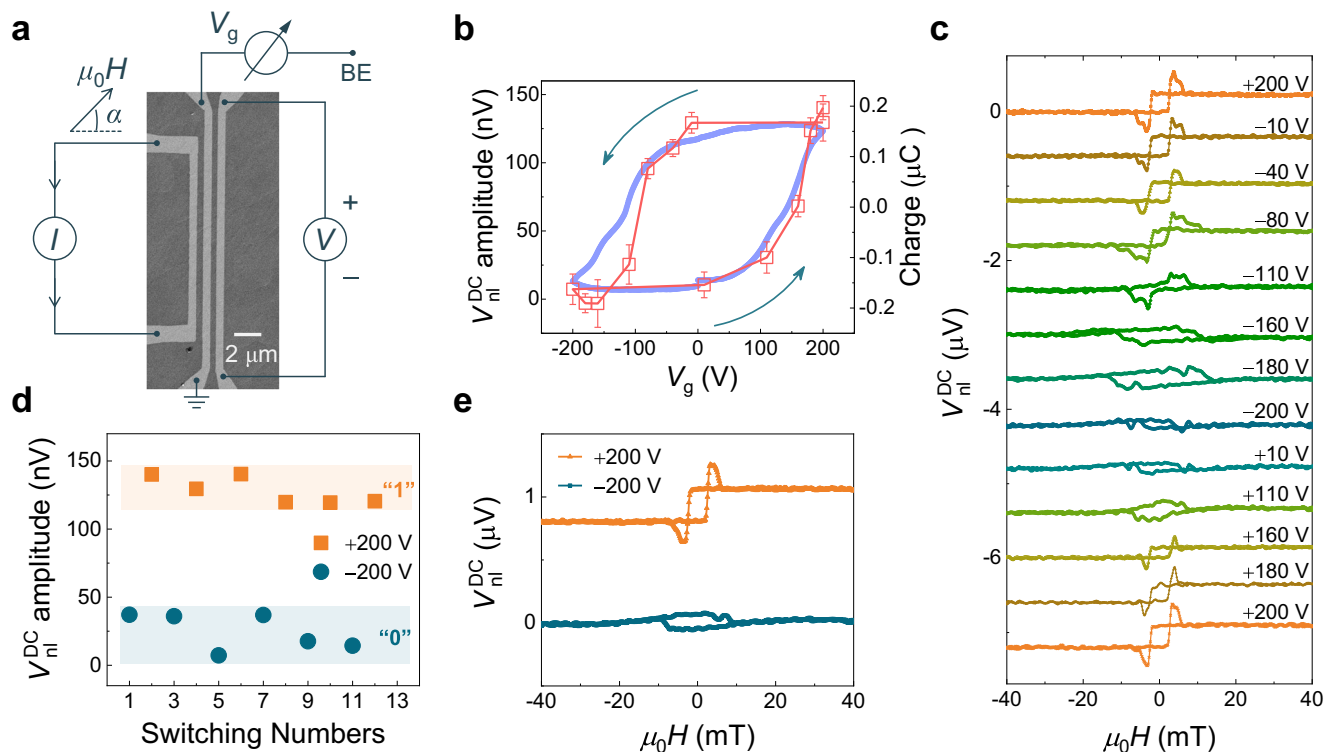


Fig. 3 | Performance of a magnon FET device. **a** SEM image of a typical three-terminal magnon FET device. V_g is applied across the G-stripe and the bottom electrode (BE). **b** Non-local voltage V_{nl}^{DC} amplitude (red) as a function of the gate voltage pulse V_g for device 1 with a width of -585 nm for the gate stripe, exhibiting a typical hysteresis in close similarity with the charge loop (blue) obtained on the same sample. Error bars are obtained from repeated measurements for each V_g . **c** Magnetic field-dependent V_{nl}^{DC} after applying different voltage pulses V_g . For

clarity, the loops are shifted vertically. All non-local measurements are conducted after the electric voltage is removed, namely, in a nonvolatile manner. **d** Electric field induced nonvolatile switching of V_{nl}^{DC} amplitude at the remnant states after applying the pulses of $V_g = \pm 200$ V. **e** The averaged magnetic field-dependent V_{nl}^{DC} for $V_g = \pm 200$ V, showing a high on/off ratio of -400%. In **b–e**, the symbols are the experimental data, and the lines are guides to the eye.

signal observed when the PMN-PT substrate is positively (negatively) polarized. Furthermore, the remnant states at $V_g = \pm 0$ V remain the same as the previous states at ± 200 V (where +0 V and -0 V correspond to the 0 V state withdrawn from +200 V and -200 V, respectively), demonstrating clear non-volatility. The turning points for V_{nl}^{DC} amplitude around -100 V and +150 V coincide with the polarization switching voltage of the PMN-PT substrate, as evidenced by the charge loop (blue curve) calculated from the polarization current loop (Supplementary Note 2). We also demonstrated a continuous toggling between two states in the magnon FET with the voltage gating. When $V_g = +200$ V is applied, the remnant state “1” results in a high V_{nl}^{DC} amplitude (above 100 nV). After switching V_g to -200 V, the remnant state “0” exhibits a low value (below 50 nV). By further cycling V_g between +200 V and -200 V, the two nonvolatile states of measured V_{nl}^{DC} amplitude exhibit no apparent attenuation. Figure 3e presents the averaged magnetic field-dependent V_{nl}^{DC} for the remnant states after ± 200 V - V_g are applied. The average on/off ratio of 6 cycles shows a high value of -400% [$(V_{nl}^{DC, +200V} - V_{nl}^{DC, -200V}) / V_{nl}^{DC, -200V} \times 100\%$, with $V_{nl}^{DC, +200V}$ ($V_{nl}^{DC, -200V}$) denotes the V_{nl}^{DC} amplitude for $V_g = +200$ V (-200 V)]. Though the minimum value of V_{nl}^{DC} is not 0, it does not impede their applications as long as the high/low states can be well-defined. This is similar to the high resistance/low resistance states in giant magnetoresistance or tunneling magnetoresistance devices, where the low resistance values are also not zero. The stability of an additional device with 21 cycles is provided in Supplementary Note 5. And the magnetic field-dependent V_{nl}^{DC} curves under higher gate voltage for a new sample are presented in Supplementary Note 6. In addition, the comparison of non-local voltage with V_g holding and removal is presented in Supplementary Note 7. Therefore, an electric

field controlled, nonvolatile three-terminal magnon FET with high on/off ratio at room temperature is demonstrated.

Discussion

We next discuss the possible mechanisms for the electric field induced modulation of the magnon current transport with device 2 (Fig. 4a, devices 2 and device 1 have similar dimensions but were prepared on different PMN-PT substrates), which exhibits a similar V_{nl}^{DC} amplitude of -150 nV for the remnant state at +0 V and a larger V_{nl}^{DC} amplitude of -70 nV for the remnant state at -0 V as compared with device 1. The different on/off ratio between device 1 (400%) and device 2 (115%) may be caused by various reasons, such as different substrate-induced variations and those caused by complicated fabrication processes. The ferroelectric substrate we used is $[\text{Pb}(\text{Mg}_{1/3}\text{Nb}_{2/3})\text{O}_3]_{(1-x)} \cdot [\text{PbTiO}_3]_x$ (PMN-PT), whose property depends sensitively on the composition. The substrate from the different positions of a wafer may have different properties, resulting in different device performance. And the YIG films may exhibit non-uniform properties after polarizing the PMN-PT substrates. In addition, the fabrication processes may also introduce discrepancies in quantity between different samples. To further reveal the role of the gap width and substrate, we performed the gate width dependent on/off ratio measurements with two series of samples fabricated on two different pieces of PMN-PT substrates (Supplementary Note 8). Furthermore, we present a summary of the on/off ratio of 16 PMN-PT/YIG/Pt samples with different YIG thicknesses, where most of the samples can achieve 20%-100% on/off ratio (Supplementary Note 9).

We first crosschecked the temperature change at both S- and D-strips since the SSE is directly proportional to the temperature

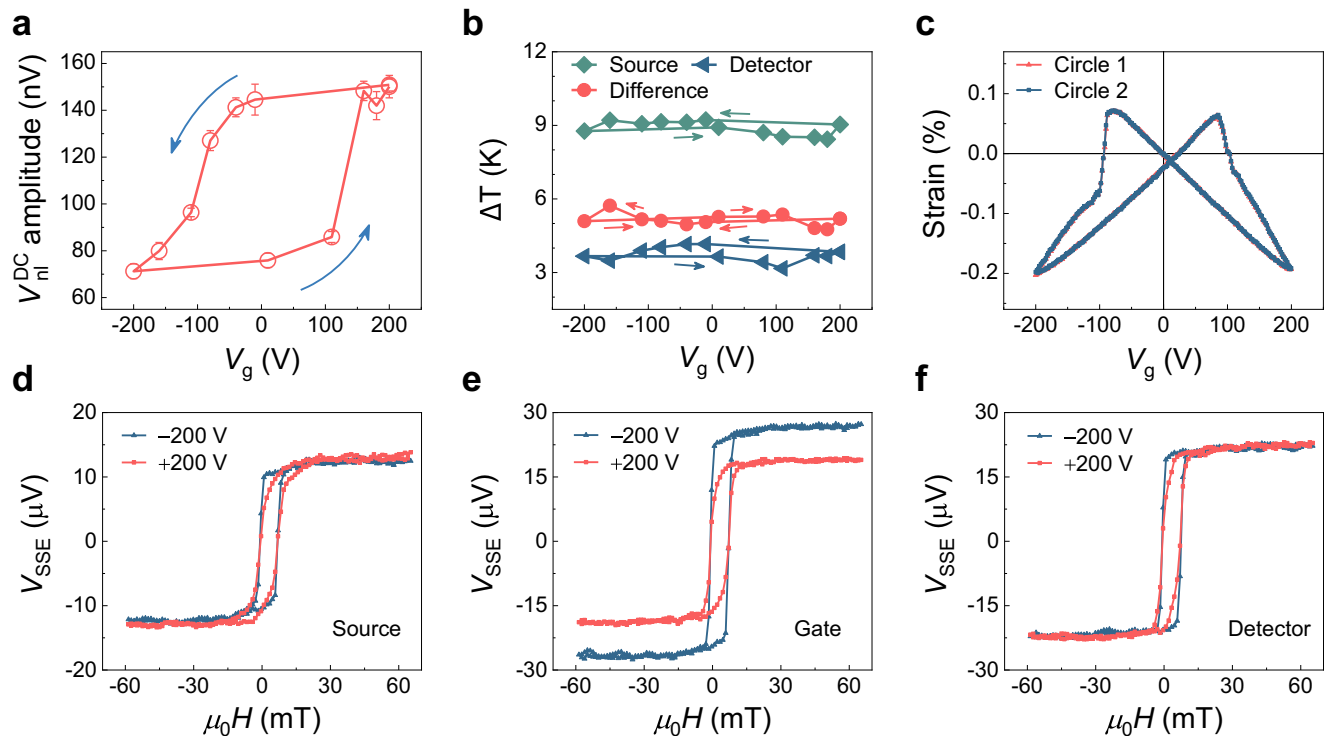


Fig. 4 | Possible mechanisms of the magnon FET device. **a** Non-local V_{ni}^{DC} amplitude as a function of the gate voltage V_g for device 2 (gate stripe width: -526 nm), with an on/off ratio of -115% for ± 200 V. Error bars are obtained from repeated measurements for each V_g . **b** Temperature variation ΔT of the S-stripe (green curve) and D-stripe (blue curve) relative to the ambient temperature for

different V_g , with a 0.5-mA DC current applied to the S-stripe. The red curve represents the temperature difference between S- and D-stripes. **c** Voltage-dependent strain curve along the [100] direction for the PMN-PT(011) substrate, exhibits a mainly symmetric butterfly-shaped feature. **d–f** Local SSE signals for three stripes of $V_g = \pm 200$ V, respectively.

difference ΔT between them. We measured the local temperature variation of these two stripes via the corresponding resistance change. With a DC electric current applied to the S-stripe, both stripes exhibit temperature increases (Fig. 4b). And the resistance remains almost constant under a certain DC current (Supplementary Note 10). Although the gate voltage pulse-dependent ΔT for both S-stripe and D-stripe exhibits a minute hysteresis loop feature, the temperature difference between them remains almost unchanged with different V_g values. Thus, we can exclude the change in temperature gradient as the dominant source for the observed gate voltage controlled magnon transport modulation. Secondly, we examined the electric field induced lattice strain. The electric field dependent strain measurement in PMN-PT(011) exhibits a typical butterfly-like feature (Fig. 4c) with a tiny remanence, which cannot explain the large nonvolatile modulation of V_{ni}^{DC} , either. Thirdly, we checked the electric field pulse dependent magnon current generation and detection efficiency at the S- and D-stripes, as well as the absorption at the G-stripe. We performed local SSE measurements for all S-, D-, and G-stripes with out-of-plane temperature gradients⁴³. After applying $V_g = \pm 200$ V at the G-stripe, the local SSE signals were almost unchanged at both S- and D-stripes (Fig. 4d, f), which indicates that the electric field at the G-stripe has little influence on both generation and detection of magnon current in the non-local geometry. Although there is a discernible difference in the local SSE signals of the G-stripe itself, the relative change ratio (-41%) is much smaller compared to the -115% ratio of V_{ni}^{DC} amplitude presented in Fig. 4a. This change actually can be attributed to the simultaneously measured resistance change of the G-stripe (5.07 k Ω for -200 V and 4.36 k Ω for +200 V) and the subsequent heating power change. Therefore, we conclude that the absorption by the G-stripe plays a minor contribution to the modulation of the lateral magnon current with the electric field gating. Furthermore, we measured the spin Hall magnetoresistance (SMR) of Pt

G-stripe with gate voltage $V_g = \pm 200$ V, and the SMR ratio of Pt/YIG is almost independent of the gate voltage (Supplementary Note 11). Since the SMR measurement indicates the reflection property of the spin current (generated in Pt) at the YIG/Pt interface, it suggests that the property of the YIG/Pt interface has no apparent change upon applying different gate voltages. In addition, we performed piezoelectric force microscopy (PFM) measurements on our PMN-PT substrate, and the results evidenced that the ferroelectric domain can be switched in a nonvolatile manner by the electric field (Supplementary Note 12), consistent with the reports in literature⁴⁴. This suggests a possible link between the modulation of the magnon transport and the change of the local electric polarization.

Since the efficiencies of the magnon current generation, detection, and absorption at both the S- and D-stripes are basically immune to the gate voltage, we attribute the modulation of V_{ni}^{DC} in our magnon-FET to the changes in magnon relaxation within the YIG channel. Although magnetoelectric coupling between YIG and PMN-PT can result in a change of magnetic anisotropy in YIG, the anisotropy change itself cannot account for the modulation of the magnon current. Firstly, in the uniform magnetic state with an external magnetic field, the anisotropy field increases the energy of the magnons with small wavevectors near the easy axis but has little influence on the energy of magnons with large wavevectors⁴⁵. As a result, the group velocity should be slower for the easy axis. One would expect that the magnon diffusion length is shorter in the direction of the magnetic easy axis rather than the reverse. Secondly, the anisotropy mainly influences the group velocity with the small wavevectors, while the energy of magnons is dominated by the exchange and dipole terms for the large wavevector. Since SSE is a broadband excitation technique with magnon frequency up to a few THz range⁴⁶, the magnons throughout the whole Brillouin zone will be thermally excited. Thus, the anisotropy change can hardly have discernible modulation on the

Table 1 | Comparison of different three-terminal lateral magnon transistors

	Materials	Working temperature	Control manner	On-off ratio	Nonvolatile
Chumak et al. ²³	YIG	300 K	Microwave	~10 ⁵ %	No
Cornelissen et al. ³¹	YIG	250 K	Current	1.6%/mA	No
Das et al. ³²	YIG	300 K	Magnetic field	18%	No
Chen et al. ²⁷	MnPS ₃	2 K	Current	∞	No
This work	YIG	300 K	Voltage	400%	Yes

magnon group velocity for the uniform magnetic state. Therefore, we speculate that the modulation of exchange stiffness and/or magnon relaxation in YIG may influence the magnon transport behavior in our magnon FET. Interestingly, anisotropic exchange stiffness has been proposed to explain the anisotropic magnon transport in ferromagnetic insulator and antiferromagnet insulator very recently^{45,47}. We propose that the modulation is due to polarization-dependent ions (Fe³⁺ or O²⁻) accumulation in the YIG layer adjacent to the interface, resulting in different coupling since Fe³⁺ is magnetic while O²⁻ is not. Dynamically, the magnon in YIG could couple with the collective excitation, such as the ferron or phonon in PMN-PT (Supplementary Note 13). A theoretical model about the influence of these couplings on the magnon transport is presented in Supplementary Note 14. Besides, noncollinear spin textures excited by magnon can induce electric dipoles^{21,22,48}, which could couple with the ferroelectric polarization of the PMN-PT substrate and influence the magnon propagation. The found large modulation of magnon flow with the electric field gating could also originate from the joint effect of multi-mechanisms. Due to differences between devices, however, it would be difficult to obtain the magnon diffusion length with different gate voltages at the present stage. Future studies like Brillouin light scattering^{49–51} or inelastic neutron scattering^{52,53} might be helpful to reveal the effect.

It is important to note that the FE substrate used in the devices discussed here has a thickness of 0.5 mm, necessitating a high voltage of 200 V for gating. It has been shown that the gate voltage can go down to the volt range when the thickness of the PMN-PT decreases down to μm range⁵⁴. It is interesting to note that PMN-PT single crystal films can be grown on silicon substrates with the thickness up to μm range⁵⁵, which is compatible with current semiconductor technology. As the strain releases with increasing thickness, it can be expected that the epitaxial PMN-PT film with μm thickness grown on a matched substrate will have similar lattice constants as the bulk PMN-PT substrate. Thus, the YIG films grown on both PMN-PT films and substrate are expected to have similar structure properties and magnon transport properties. The growth temperature of high-quality PMN-PT film, however, is beyond the maximum temperature that we can reach in our sputtering system. Instead, we deposited a 400-nm PZT (PbZr_{0.52}Ti_{0.48}O₃) film on an Nb-doped SrTiO₃(001) substrate and further prepared a magnon field effect transistor. This device exhibits ~28% on/off ratio under ± 10 V gate voltages (Supplementary Note 15). Furthermore, the current devices have been demonstrated at a lateral size of a few μm . Given that the magnon current exhibits exponential decay with propagation distance and the gating only requires switching of an FE domain, it can be anticipated that the device can be readily scaled down in lateral size.

Lastly, we briefly compare the reported three-terminal lateral magnon transistors so far. Ideally, a good magnon transistor candidate should have a large on/off ratio for sensitivity, can be triggered by electric field and be nonvolatile for energy efficiency, and work in a

wide temperature range including room temperature. As summarized in Table 1, some reported devices either have large on/off ratio^{23,27} or have room temperature functionality^{23,32}. But none of them possesses all the above-mentioned characters of an ideal magnon transistor as presented in this work. Thus, our demonstrated device has clear advantages in comparison with previously reported ones.

In conclusion, we have successfully shown that the magnon transport in a structure consisting of a ferrimagnetic/ferroelectric insulator bilayer can be efficiently controlled by an electric field at room temperature, achieving a high on/off ratio of ~400%. This achievement represents the realization of the long-awaited three-terminal magnon field effect transistor. In combination with the nonvolatility nature of the device, the ability to manipulate magnon transport using an electric field provides significant advantages in terms of energy efficiency. These findings open up new possibilities for the development of energy-efficient magnon based logic devices and hold promising potential in unconventional computing schemes like neuromorphic computing.

Methods

Device fabrication

The ~60-nm YIG films were deposited on PMN-PT(011) substrates with RF magnetron sputtering with a post-annealing under 800 °C for 4 h in air atmosphere. Three Pt stripes with a thickness of 3.5 nm (lateral dimensions of ~550 nm × 15 μm) were fabricated using e-beam lithography, DC magnetron sputtering, and lift-off techniques. Finally, Ti(5 nm)/Au(100 nm) and Ti(5 nm)/Au(200 nm) stripes were successively prepared with DC magnetron sputtering and lift-off techniques as the top and bottom electrodes, respectively. All depositions were performed at room temperature. The 400-nm PZT films were deposited on Nb-doped SrTiO₃ (001) substrate by RF magnetron sputtering with the following conditions: 550 °C, Ar/O₂ ratio of 15/1, and a total pressure of 10 mTorr.

Electric characterization

All electric measurements were performed at room temperature using our home-built transport measurements system with a rotatable magnetic field. **Harmonic non-local measurement.** An AC current with the amplitude $I_{\omega} = 0.71$ mA and frequency $f = 15.7$ Hz was injected into the S-stripe with a Keithley 6221 current source, and the first-harmonic and second-harmonic signals at D-stripe were measured by an SR860 lock-in amplifier from Stanford Research Systems. **DC non-local measurement.** A DC current was supplied to the S-stripe with a Keithley 6221 current source, and the voltage across the D-stripe was measured by a Keithley 2182A voltmeter. The electric field between the G-stripe and bottom electrode was applied by a Keithley 2400 source meter. All measurements were performed after the gate voltage is removed. **Local spin Seebeck effect (SSE) measurement.** The local SSE signals were obtained by applying AC current $I_{\omega} = 0.50$ mA with frequency $f = 1.37$ kHz to each stripe and detecting the second-harmonic signal by an SR860 lock-in amplifier. **Piezoelectric force microscopy (PFM) measurement.** The ferroelectric domain switching measurements of our PMN-PT single crystal substrate were performed by PFM (Bruker, Dimension Icon).

Data availability

All data supporting the findings of this study are available within the main text and the Supplementary Information file. The data that support the findings of this study are available from the corresponding authors upon reasonable request. Source data are provided with this paper.

References

1. Waldrop, M. M. The chips are down for Moore's law. *Nature* **530**, 144–147 (2016).

2. Chumak, A. V., Vasyuchka, V. I., Serga, A. A. & Hillebrands, B. Magnon spintronics. *Nat. Phys.* **11**, 453–461 (2015).
3. Cornelissen, L. J., Liu, J., Duine, R. A., Youssef, J. B. & van Wees, B. J. Long-distance transport of magnon spin information in a magnetic insulator at room temperature. *Nat. Phys.* **11**, 1022–1026 (2015).
4. Kajiwara, Y. et al. Transmission of electrical signals by spin-wave interconversion in a magnetic insulator. *Nature* **464**, 262–266 (2010).
5. Du, C. et al. Control and local measurement of the spin chemical potential in a magnetic insulator. *Science* **357**, 195–198 (2017).
6. Goennenwein, S. T. B. et al. Non-local magnetoresistance in YIG/Pt nanostructures. *Appl. Phys. Lett.* **107**, 172405 (2015).
7. Li, J. et al. Observation of magnon-mediated current drag in Pt/yttrium iron garnet/Pt(Ta) trilayers. *Nat. Commun.* **7**, 10858 (2016).
8. Han, J., Zhang, P., Hou, J. T., Siddiqui, S. A. & Liu, L. Mutual control of coherent spin waves and magnetic domain walls in a magnonic device. *Science* **366**, 1121–1125 (2019).
9. Yu, H., Xiao, J. & Schultheiss, H. Magnetic texture based magnonics. *Phys. Rep.* **905**, 1–59 (2021).
10. Pirro, P., Vasyuchka, V. I., Serga, A. A. & Hillebrands, B. Advances in coherent magnonics. *Nat. Rev. Mater.* **6**, 1114–1135 (2021).
11. Wang, Y. et al. Magnetization switching by magnon-mediated spin torque through an antiferromagnetic insulator. *Science* **366**, 1125–1128 (2019).
12. Haldar, A., Tian, C. & Adeyeye, A. O. Isotropic transmission of magnon spin information without a magnetic field. *Sci. Adv.* **3**, e1700638 (2017).
13. Richardson, D., Kalinikos, B. A., Carr, L. D. & Wu, M. Spontaneous Exact Spin-Wave Fractals in Magnonic Crystals. *Phys. Rev. Lett.* **121**, 107204 (2018).
14. Khitun, A., Bao, M. & Wang, K. L. Magnonic logic circuits. *J. Phys. D: Appl. Phys.* **43**, 264005 (2010).
15. Chumak, A. V., Serga, A. A. & Hillebrands, B. Magnonic crystals for data processing. *J. Phys. D: Appl. Phys.* **50**, 244001 (2017).
16. Csaba, G., Papp, Á. & Porod, W. Perspectives of using spin waves for computing and signal processing. *Phys. Lett. A* **381**, 1471–1476 (2017).
17. Liu, C. et al. Long-distance propagation of short-wavelength spin waves. *Nat. Commun.* **9**, 738 (2018).
18. Editorial. The next wave. *Nat. Phys.* **11**, 437–437 (2015).
19. Yuan, H. Y., Cao, Y., Kamra, A., Duine, R. A. & Yan, P. Quantum magnonics: When magnon spintronics meets quantum information science. *Phys. Rep.* **965**, 1–74 (2022).
20. Dong, S., Liu, J.-M., Cheong, S.-W. & Ren, Z. Multiferroic materials and magnetoelectric physics: symmetry, entanglement, excitation, and topology. *Adv. Phys.* **64**, 519–626 (2015).
21. Mills, D. L. & Dzyaloshinskii, I. E. Influence of electric fields on spin waves in simple ferromagnets: Role of the flexoelectric interaction. *Phys. Rev. B* **78**, 184422 (2008).
22. Zhang, X., Liu, T., Flatté, M. E. & Tang, H. X. Electric-Field Coupling to Spin Waves in a Centrosymmetric Ferrite. *Phys. Rev. Lett.* **113**, 037202 (2014).
23. Chumak, A. V., Serga, A. A. & Hillebrands, B. Magnon transistor for all-magnon data processing. *Nat. Commun.* **5**, 4700 (2014).
24. Lebrun, R. et al. Tunable long-distance spin transport in a crystalline antiferromagnetic iron oxide. *Nature* **561**, 222–225 (2018).
25. Wright, K. Focus: A Trio of Magnon Transistors. *Physics* **11**, 23 (2018).
26. Liu, C. et al. Electric field control of magnon spin currents in an antiferromagnetic insulator. *Sci. Adv.* **7**, eabg1669 (2021).
27. Chen, G. et al. Electrically switchable van der Waals magnon valves. *Nat. Commun.* **12**, 6279 (2021).
28. Yu, T., Cai, C. & Bauer, G. E. W. Chirality Enables Thermal Magnon Transistors. *Sci. China Phys. Mech. Astron.* **67**, 247511 (2024).
29. Zhou, Y. et al. Piezoelectric Strain-Controlled Magnon Spin Current Transport in an Antiferromagnet. *Nano Lett.* **22**, 4646–4653 (2022).
30. Parsonnet, E. et al. Nonvolatile Electric Field Control of Thermal Magnons in the Absence of an Applied Magnetic Field. *Phys. Rev. Lett.* **129**, 087601 (2022).
31. Cornelissen, L. J., Liu, J., van Wees, B. J. & Duine, R. A. Spin-Current-Controlled Modulation of the Magnon Spin Conductance in a Three-Terminal Magnon Transistor. *Phys. Rev. Lett.* **120**, 097702 (2018).
32. Das, K. S., Feringa, F., Middelkamp, M., van Wees, B. J. & Veramarun, I. J. Modulation of magnon spin transport in a magnetic gate transistor. *Phys. Rev. B* **101**, 054436 (2020).
33. Santos, O. A., Feringa, F., Das, K. S., Youssef, J. B. & van Wees, B. J. Efficient Modulation of Magnon Conductivity in $\text{Y}_3\text{Fe}_5\text{O}_{12}$ Using Anomalous Spin Hall Effect of a Permalloy Gate Electrode. *Phys. Rev. Appl.* **15**, 014038 (2021).
34. Zhi, B. et al. Electric-Field-Modulated Nonvolatile Resistance Switching in $\text{VO}_2/\text{PMN-PT}(111)$ Heterostructures. *ACS Appl. Mater. Interfaces* **6**, 4603–4608 (2014).
35. Yang, Y. et al. Controlling the anomalous Hall effect by electric-field-induced piezo-strain in $\text{Fe}_{40}\text{Pt}_{60}/(001)\text{-Pb}(\text{Mg}_{1/3}\text{Nb}_{2/3})_{0.67}\text{Ti}_{0.33}\text{O}_3$ multiferroic heterostructures. *Appl. Phys. Lett.* **112**, 033506 (2018).
36. Yan, H. et al. A piezoelectric, strain-controlled antiferromagnetic memory insensitive to magnetic fields. *Nat. Nanotechnol.* **14**, 131–136 (2019).
37. Zheng, M. et al. Ferroelastic strain control of multiple nonvolatile resistance tuning in $\text{SrRuO}_3/\text{PMN-PT}(111)$ multiferroic heterostructures. *Appl. Phys. Lett.* **110**, 182403 (2017).
38. Cheng, J. et al. Quantitative estimation of thermoelectric contributions in spin pumping signals through microwave photoresistance measurements. *Phys. Rev. B* **103**, 014415 (2021).
39. Gui, Y. S., Mecking, N., Wirthmann, A., Bai, L. H. & Hu, C. M. Electrical detection of the ferromagnetic resonance: Spin-rectification versus bolometric effect. *Appl. Phys. Lett.* **91**, 082503 (2007).
40. Gomez-Perez, J. M., Vélez, S., Hueso, L. E. & Casanova, F. Differences in the magnon diffusion length for electrically and thermally driven magnon currents in $\text{Y}_3\text{Fe}_5\text{O}_{12}$. *Phys. Rev. B* **101**, 184420 (2020).
41. Jin, H., Boona, S. R., Yang, Z., Myers, R. C. & Heremans, J. P. Effect of the magnon dispersion on the longitudinal spin Seebeck effect in yttrium iron garnets. *Phys. Rev. B* **92**, 054436 (2015).
42. Wang, L., Wang, X. & Shi, J. Measurement and Estimation of Ferroelectric Hysteresis Loops. *Ferroelectrics* **411**, 86–92 (2010).
43. Chen, Y. et al. First harmonic measurements of the spin Seebeck effect. *Appl. Phys. Lett.* **113**, 202403 (2018).
44. Liu, M. et al. Non-volatile ferroelastic switching of the Verwey transition and resistivity of epitaxial $\text{Fe}_3\text{O}_4/\text{PMN-PT}(011)$. *Sci. Rep.* **3**, 1876 (2013).
45. Li, R. et al. Anisotropic Magnon Spin Transport in Ultrathin Spinel Ferrite Thin Films—Evidence for Anisotropy in Exchange Stiffness. *Nano Lett.* **22**, 1167–1173 (2022).
46. Barker, J. & Bauer, G. E. W. Thermal Spin Dynamics of Yttrium Iron Garnet. *Phys. Rev. Lett.* **117**, 217201 (2016).
47. Das, S. et al. Anisotropic long-range spin transport in canted antiferromagnetic orthoferrite YFeO_3 . *Nat. Commun.* **13**, 6140 (2022).
48. Xia, J., Zhang, X., Liu, X., Zhou, Y. & Ezawa, M. Universal Quantum Computation Based on Nanoscale Skyrmion Helicity Qubits in Frustrated Magnets. *Phys. Rev. Lett.* **130**, 106701 (2023).
49. Hamrle, J. et al. Determination of exchange constants of Heusler compounds by Brillouin light scattering spectroscopy: application to Co_2MnSi . *J. Phys. D: Appl. Phys.* **42**, 084005 (2009).
50. Belmeugeni, M. et al. Microstrip line ferromagnetic resonance and Brillouin light scattering investigations of magnetic properties of Co_2MnGe Heusler thin films. *Phys. Rev. B* **79**, 024419 (2009).
51. Haldar, A., Banerjee, C., Laha, P. & Barman, A. Brillouin light scattering study of spin waves in NiFe/Co exchange spring bilayer films. *J. Appl. Phys.* **115**, 133901 (2014).

52. Dai, P., Fernandez-Baca, J. A., Plummer, E. W., Tomioka, Y. & Tokura, Y. Magnetic coupling in the insulating and metallic ferromagnetic $\text{La}_{1-x}\text{Ca}_x\text{MnO}_3$. *Phys. Rev. B* **64**, 224429 (2001).
53. Naser, H., Rado, C., Lapertot, G. & Raymond, S. Anisotropy and temperature dependence of the spin-wave stiffness in $\text{Nd}_2\text{Fe}_{14}\text{B}$: An inelastic neutron scattering investigation. *Phys. Rev. B* **102**, 014443 (2020).
54. Kum, H. S. et al. Heterogeneous integration of single-crystalline complex-oxide membranes. *Nature* **578**, 75–81 (2020).
55. Baek, S. H. et al. Giant Piezoelectricity on Si for Hyperactive MEMS. *Science* **334**, 958–961 (2011).

Acknowledgements

We thank Prof. Peng Yan for fruitful discussions and the staff at BLO7U beamline of Shanghai Synchrotron Radiation Facility (SSRF) for the film growth. This work was supported by the National Key R&D Program of China (Grant No. 2022YFA1403601, 2018YFA0306004, 2023YFC2410501, 2022YFA1402700), the National Natural Science Foundation of China (Grants No. 92165103, No. 12274204, No. 12274203, No. 12104468, No. 51971110, No. 12241402, No. 12474059, No.12404137, No.12374113), the Natural Science Foundation of Jiangsu Province (Grant No. BK20241254), the Jiangsu Funding Program for Excellent Postdoctoral Talent (No. 2024ZB786).

Author contributions

J.C., R.Y., L.S. contributed equally to this work. H.F.D. supervised the project. J.C., R.Y., L.S., K.H., X.Y. grew the films. J.C., R.Y. prepared the pattern with the lithography. J.C., R.Y., B.F.M., M.Y., Z.Y.Z. performed the measurements. X.L.H., F.Z.H., X.M.L. made the contribution of the PFM measurements and analysis. P.C., H.L.C. performed the ferroelectric measurements and analysis. J.C., R.Y., B.F.M., L.S., H.F.D. analyzed the data. H.Y.Y., J.C., H.F.D. proposed a possible mechanism for the coupling of ferrimagnetic insulator and ferroelectric material. J.C., R.Y., L.S., K.H., T.Z.J., M.Y., Z.Y.Z., X.L.H., H.N., X.Y., P.C., G.C., J.X., F.Z.H., X.M.L., H.L.C., H.Y.Y., B.F.M., and H.F.D. participated the discussions. J.C., R.Y., B.F.M., L.S., H.F.D. wrote the original manuscript. All authors contributed to the interpretation and editing of the manuscript.

Competing interests

The authors declare no competing interests.

Additional information

Supplementary information The online version contains supplementary material available at <https://doi.org/10.1038/s41467-024-53524-7>.

Correspondence and requests for materials should be addressed to Huaiyang Yuan, Bingfeng Miao or Haifeng Ding.

Peer review information *Nature Communications* thanks Lichuan Jin and the other anonymous reviewer(s) for their contribution to the peer review of this work. A peer review file is available.

Reprints and permissions information is available at <http://www.nature.com/reprints>

Publisher's note Springer Nature remains neutral with regard to jurisdictional claims in published maps and institutional affiliations.

Open Access This article is licensed under a Creative Commons Attribution-NonCommercial-NoDerivatives 4.0 International License, which permits any non-commercial use, sharing, distribution and reproduction in any medium or format, as long as you give appropriate credit to the original author(s) and the source, provide a link to the Creative Commons licence, and indicate if you modified the licensed material. You do not have permission under this licence to share adapted material derived from this article or parts of it. The images or other third party material in this article are included in the article's Creative Commons licence, unless indicated otherwise in a credit line to the material. If material is not included in the article's Creative Commons licence and your intended use is not permitted by statutory regulation or exceeds the permitted use, you will need to obtain permission directly from the copyright holder. To view a copy of this licence, visit <http://creativecommons.org/licenses/by-nc-nd/4.0/>.

© The Author(s) 2024